NeuroImage 274 (2023) 120124

Contents lists available at ScienceDirect

NeuroImage

journal homepage: www.elsevier.com/locate/neuroimage

Higher order diffusion imaging as a putative index of human sleep-related microstructural changes and glymphatic clearance

Balázs Örzsik[a,b,*], Marco Palombo[c,d], Iris Asllani[b,e], Derk-Jan Dijk[f,g], Neil A. Harrison[c], Mara Cercignani[c]

[a] Radiology, Leiden University Medical Center, Leiden, the Netherlands
[b] CISC, Brighton and Sussex Medical School, Brighton, United Kingdom
[c] CUBRIC, Cardiff University, United Kingdom
[d] School of Computer Science and Informatics, Cardiff University, Cardiff, UK
[e] Rochester Institute of Technology, New York, United States
[f] Surrey Sleep Research Centre, Faculty of Health and Medical Sciences, University of Surrey, Guildford UK
[g] UK Dementia Research Institute Care Research and Technology Centre, Imperial College London and the University of Surrey, Guildford UK

ARTICLE INFO

Key words:
Diffusion MRI
Diffusion Kurtosis
Sleep
Glymphatic system

ABSTRACT

The brain has a unique macroscopic waste clearance system, termed the glymphatic system which utilises perivascular tunnels surrounded by astroglia to promote cerebrospinal-interstitial fluid exchange. Rodent studies have demonstrated a marked increase in glymphatic clearance during sleep which has been linked to a sleep-induced expansion of the extracellular space and concomitant reduction in intracellular volume. However, despite being implicated in the pathophysiology of multiple human neurodegenerative disorders, non-invasive techniques for imaging glymphatic clearance in humans are currently limited.

Here we acquired multi-shell diffusion weighted MRI (dwMRI) in twenty-one healthy young participants (6 female, 22.3 ± 3.2 years) each scanned twice, once during wakefulness and once during sleep induced by a combination of one night of sleep deprivation and 10 mg of the hypnotic zolpidem 30 min before scanning. To capture hypothesised sleep-associated changes in intra/extracellular space, dwMRI were analysed using higher order diffusion modelling with the prediction that sleep-associated increases in interstitial (extracellular) fluid volume would result in a decrease in diffusion kurtosis, particularly in areas associated with slow wave generation at the onset of sleep.

In line with our hypothesis, we observed a global reduction in diffusion kurtosis (t_{15}=2.82, $p = 0.006$) during sleep as well as regional reductions in brain areas associated with slow wave generation during early sleep and default mode network areas that are highly metabolically active during wakefulness. Analysis with a higher-order representation of diffusion (MAP-MRI) further indicated that changes within the intra/extracellular domain rather than membrane permeability likely underpin the observed sleep-associated decrease in kurtosis. These findings identify higher-order modelling of dwMRI as a potential new non-invasive method for imaging glymphatic clearance and extend rodent findings to suggest that sleep is also associated with an increase in interstitial fluid volume in humans.

Abbreviations: AD, axial diffusivity; ADC, apparent diffusion coefficient; AK, axial kurtosis; ASL, arterial spin labelling; CSF, cerebrospinal fluid; DKI, diffusion kurtosis imaging; DMN, default mode network; DTI, diffusion tensor imaging; dwMRI, diffusion weighted magnetic resonance imaging; EEG, electroencephalography; FA, fractional anisotropy; FDR, false discovery rate; FIR, finite impulse response; fMRI, functional magnetic resonance imaging; FOV, field of view; FWHM, full width half maximum; GM, grey matter; GRAPPA, generalised autocalibrating partial parallel acquisition; HF, high frequency; HRV, heart rate variability; ISF, interstitial fluid; KFA, kurtosis fractional anisotropy; KSS, Karolinska sleepiness scale; MAP-MRI, mean apparent propagator magnetic resonance imaging; MD, mean diffusivity; MK, mean kurtosis; MKT, mean kurtosis tensor; MNI, Montreal neurological institute; MPRAGE, magnetisation prepared rapid gradient echo; MRI, magnetic resonance imaging; MSD, mean squared displacement; NG, non-Gaussianity; NREM, non-rapid eye movement; PSQI, Pittsburgh sleep quality index; QIV, Q-space inverse variance; RK, radial diffusivity; RK, radial kurtosis; RTAP, return to axis probability; RTOP, return to origin probability; RTPP, return to plane probability; SPM, statistical parametric mapping; SWS, slow wave sleep; TE, echo time; TR, repetition time; VBM, Voxel-based morphometry; WM, white matter.

* Corresponding author at: Radiology, Leiden University Medical Center, Leiden, Albinusdreef 2, Leiden, ZA 2333, the Netherlands.
E-mail address: bo80@sussex.ac.uk (B. Örzsik).

https://doi.org/10.1016/j.neuroimage.2023.120124.
Received 23 January 2023; Received in revised form 16 March 2023; Accepted 18 April 2023
Available online 20 April 2023.

1. Introduction

Clearance of cellular metabolites and other solutes is critical to the maintenance of cell homoeostasis. In peripheral tissues, this is achieved by lymph vessels (Liao and Padera, 2013). However, the brain lacks a conventional lymphatic system and is instead believed to achieve waste clearance by using convective influx of cerebrospinal fluid (CSF) through the periarterial space which then exchanges with parenchymal interstitial fluid (ISF) (Iliff et al., 2012; Iliff and Nedergaard, 2013). First described by Nedergaard and colleagues, this macroscopic waste clearance system has been named the 'glymphatic system'. Though the glymphatic hypothesis has gained momentum, other complementary systems have also been proposed for brain clearance (see Tarasoff-Conway et al., 2015 for a recent review).

Preclinical studies have demonstrated that glymphatic clearance is particularly active during sleep (Xie et al., 2013; Ding et al., 2016). For example, during both anaesthesia and natural sleep fluorescent dye injected into the cisterna magna rapidly appears along the periarterial spaces and then the parenchymal space (Xie et al., 2013; Iliff et al., 2012). This study also reported a ~60% increase in interstitial volume fraction during slow wave sleep (SWS) in mice, leading to the proposition that this sleep-associated expansion of the interstitial space facilitates exchange of CSF with ISF by reducing resistance to flow (Xie et al., 2013; Ding et al., 2016). This expansion of the interstitial space has been partially attributed to a sleep-associated reduction in noradrenergic signalling, the major driver for arousal (Xie et al., 2013; Berridge and Waterhouse, 2003; Osorio-Forero et al., 2022). Evidence for an increase in glymphatic flow during slow wave sleep has also been recently reported in humans using simultaneous EEG/ fMRI, where a correlation between slow wave delta activity and CSF flow into the fourth ventricle was observed (Fultz et al., 2019). Beyond its physiological role, the glymphatic system has also been implicated in the clearance of proteins such as amyloid-beta linked to neurodegenerative disorders such as Alzheimer's disease (Iliff et al., 2012, 2014; Plog et al., 2015; Peng et al., 2016; Arbel-Ornath et al., 2013; Nedergaard and Goldman, 2020).

Approaches for visualising glymphatic flow in rodents typically involve the direct injection of labelled tracers such as fluorescent dyes, radio-labelled isotopes, or gadolinium into the CSF spaces, then measuring their spatio-temporal distribution (Iliff et al., 2012; Gaberel et al., 2014; Eide and Ringstad, 2015). A handful of human studies have been able to adopt a similar methodology in the context of known pathology such as CSF leaks or idiopathic normal pressure hydrocephalus. In agreement with findings in rodents, human injection studies also reported a brain-wide parenchymal contrast enhancement following intra-thecal gadolinium injection (Eide and Ringstad, 2015; Ringstad et al., 2017; Eide et al., 2018). However, due to their invasive nature this approach is poorly suited for more widespread adoption in human in-vivo studies.

To date, approaches for non-invasively imaging the glymphatic system have predominantly focussed on developing techniques that can quantify CSF flow (Fultz et al., 2019), identify brain oscillations associated with the forces driving brain clearance with magnetic resonance encephalography (Helakari et al., 2022) or use conventional diffusion weighted MRI (dwMRI) to detect changes in water compartmentalization, exploiting the observation that glymphatic clearance modulates the relative sizes of the intracellular, interstitial and CSF fluid compartments (Demiral et al., 2019). The latter have almost exclusively focused on Gaussian diffusion, pseudo-diffusion, and low b values (Taoka et al., 2017; Demiral et al., 2019). However, in other disorders associated with subtle changes in intra/extracellular volume such as acute stroke, adoption of high b-value ($\geq$2000 smm^{-2}) diffusion weighted images coupled with higher order diffusion models such as diffusion kurtosis imaging (DKI) (Jensen et al., 2005), have demonstrated superior sensitivity (Jenesen et al., 2011; Grinberg et al., 2012; Hui et al., 2012). As an example, stroke-associated cell swelling (due to acute failure of the Na^+/K^+-pump) leads to an increase in interstitial space tortuosity and consequently increased diffusion kurtosis (Tao et al., 2005).

Here, we therefore hypothesise that the expansion of interstitial space expected with sleep would result in a reduction in diffusion non-Gaussianity and hence diffusion kurtosis. We additionally expect that sleep-related changes would be more pronounced in brain regions associated with slow wave activity during early sleep. To test our hypothesis, we acquired multi-directional high b-value (>2000 smm^{-2}) diffusion weighted images in a cohort of twenty-one healthy volunteers each scanned twice (awake and asleep) and analysed the data with diffusion kurtosis imaging (DKI) (Jensen et al., 2005), as well as with mean apparent propagator MRI (MAP-MRI), a higher order representation (Özarslan et al., 2013).

2. Materials and methods

2.1. Study design

We utilised a within-subject cross-over design in which all participants underwent two scanning sessions (once awake and once during sleep) separated by 3–7 days (mean 4.0 days). Participants underwent an initial screening and individuals with any current neurological or psychiatric illness, use of prescribed medication, contraindication to zolpidem or history of sleep disorders were excluded. Heavy smokers (>5 cigarettes a day) were excluded. Daily caffeine intake was not part of the exclusion criteria, however participants were asked not to consume caffeine for 12 h prior to the scanning sessions.

Participants then completed the Pittsburgh Sleep Quality Index (PSQI) (Buysse et al., 1989) and only those with a self-reported regular sleep cycle and sleep efficiency >80% were recruited. Twenty-one healthy individuals (6 females, mean age 22.3 ± 3.2 years) passed screening and were given an Actigraphy watch to wear (Actiwatch Spectrum Plus, Philips Respironics) prior to each scanning session. Ethical approval was obtained from the Brighton and Sussex Medical School Research Governance and Ethics Committee (ER/BO80/1) and was in accordance with the Declaration of Helsinki. All subjects gave informed written consent before participating in the study.

Both scanning sessions were scheduled for the same time of the day: 09:44 min (±22 m) to minimise circadian effects. For the awake session, participants were instructed to arrive at the imaging centre well rested after a full night sleep. For the sleep session, they were instructed to remain awake the night before scanning (~24 h sleep deprivation) then administered 10 mg zolpidem 30-min prior to the scheduled MRI scan. Zolpidem is one of the most widely prescribed short-acting (with a half-life of 1.5- 2.4 h) hypnotic drugs and has been shown to be efficacious in inducing and maintaining sleep with minimal dependence liability or toxicity (Priest et al., 1997; Monti et al., 2017). 10 mg is a standard dose for non-elderly individuals, which reaches peak plasma concentration in ~45 min (Priest et al., 1997; Monti et al., 2017). Participants were requested to avoid caffeinated beverages and nicotine for 12 h prior to each scan. Total sleep time, sleep efficiency prior to the wake scan and compliance with sleep deprivation before the sleep scan were assessed using Actigraphy data and sleepiness immediately prior to each scanning session was assessed using the Karolinska Sleepiness Scale (KSS) (Åkerstedt and Gillberg, 1990). Participants chose the session order (Fourteen (67%) started with the wake scan). Sleep efficiency is a measure of sleep quality calculated as the ratio of total sleep time over total time spent in bed.

During scanning, participants were instructed to maintain light pressure on a button box (to detect loss of muscle tone at sleep onset) with responses recorded using a custom Matlab script (MathWorks, Natick, Massachusetts, United States). Respiration and pulse were continuously monitored with a respiration belt (Biopac Systems UK) and pulse-oxymeter (Nonin 8600FO) and data recorded with Biopac AcqKnowledge 5 software (Biopac Systems UK). After scanning participants completed a subjective sleep questionnaire using a likert scale to indicate how sleepy, when, how long and how deeply they think they slept during each scan.

2.2. MRI acquisition

MRI data were acquired on a Siemens Prisma 3T scanner equipped with a 32-channel head coil. Diffusion weighted MRI measurement were acquired with 2 shells (b = 800, 2600 s/mm^2), sampled in 32 and 64 directions respectively with a single shot, twice-refocused spin echo (Reese et al., 2003) and an echo planar readout, TR=4100 ms, TE=87 ms, flip angle=90°, FOV=240 × 240 mm^2, matrix=96 × 96, slices = 60, slice thickness = 2.5 mm, multiband factor = 2, GRAPPA reduction factor = 2, partial Fourier 6/8. Nine b = 0 s/mm^2 vol were also acquired. Data were acquired with anterior-to-posterior phase encoding, and a single b0 (b = 0 s/mm^2) image was also acquired with posterior-to-anterior phase encoding to calculate the susceptibility induced off-resonance field. A total of 105 dwMRI volumes were acquired (9 + 32+64), the duration of the diffusion scan was approximately 8 min. A T_1-weighted magnetization-prepared rapid gradient echo (MPRAGE) TR=2300 ms, TE=2.19 ms, TI=920 ms, flip angle=9°, field of view (FOV): 256 × 256 × 192 mm^3, resolution: 1 mm^3 was acquired for normalisation purposes. Total time spent in the scanner was 60 min, of which the first 40 min was sodium MRI followed immediately (after changing the sodium coil, which took ~2 min) by 20 min of proton scanning. The proton scans included high resolution T_1-weighted (MPRAGE) anatomical imaging (5.5 min), diffusion weighted imaging (8 min) and arterial spin labelling (3.5 min), in that order.

2.3. Analysis of physiological measures

Interbeat intervals were derived from RR peaks then imported into the Kubios software package, to calculate heart rate and parasympathetically mediated high frequency heart rate variability (HF-HRV) for contiguous 5-mins. Respiration data was bandpass filtered (finite impulse response (FIR): 0.05 Hz to 1 Hz) and the Biopac "find cycles" function applied to detect inspiration peaks. Inspiration peak time intervals were then calculated and imported into a custom Matlab script to determine mean respiration rate in 5-min contiguous epochs.

2.4. MRI data processing

Diffusion weighted images were first corrected for susceptibility induced distortions using the *FSL TopUp* function (FSL, version 6.0.1) followed by *eddy* to compensate for rigid body and eddy current induced distortions (Andersson and Sotiropoulos, 2016). To address motion-associated signal dropout, we estimated and replaced slice-wise outliers using Gaussian Process prediction (Andersson et al., 2016) then applied additional slice-to-volume motion correction by modelling movement as a piecewise continuous function over time (Andersson et al., 2017).

2.4.1. Diffusion kurtosis imaging and diffusion kurtosis tensor imaging (DKI/DKTI)

As recommended by the DIPY library creators, a 3D Gaussian smoothing kernel (FWHM=1.25 mm) was applied to the diffusion weighted images then the DKI/DKTI model fitted using the *DiffusionKurtosisModel* from the DIPY library (Garyfallidis et al., 2014). This produced 5 kurtosis images: mean kurtosis (MK), axial kurtosis (AK), radial kurtosis (RK), mean kurtosis tensor (MKT), and kurtosis fractional anisotropy (KFA), note that the latter 2 come from the DKTI model. Moreover, the DKI model produced 4 conventional diffusion tensor imaging (DTI) images: mean diffusivity (MD), axial diffusivity (AD), radial diffusivity (RD) and fractional anisotropy (FA).

Images were then co-registered to their corresponding high resolution MPRAGE image using Statistical Parametric Mapping (SPM12, Wellcome Trust Centre for Neuroimaging). The normalization parameters obtained from the segmentation (SPM12) of the high-resolution anatomical image were used to warp the DKI/DKTI images into MNI space. 3D Gaussian smoothing (SPM12) with FWHM=6 mm was applied to the normalized images prior to voxel-wise comparison. Global measures were obtained by applying GM and WM masks (tissue probability>90%) to the wake and sleep images in high resolution space.

2.4.2. Mean apparent propagator mri (MAP-MRI)

Changes in diffusion kurtosis may result from changes in either: (1) the intra/extra cellular compartment size (Fieremans et al., 2010; Aggarwal et al., 2020) or (2) exchange between compartments (Jelescu et al., 2022; Olesen et al., 2022). To address this, we additionally processed the diffusion-weighted images with MAP-MRI (Özarslan et al., 2013) using the DIPY library (Garyfallidis et al., 2014) with laplacian regularisation (weighting factor: 0.2) for fitting (Fick et al., 2016). This produced parametric images of: Mean Squared Displacement (MSD), Q-space Inverse Variance (QIV), Return to origin probability (RTOP), Return to axis probability (RTAP) and Return to plane probability (RTPP). RTOP, RTAP and RTPP images were normalised by the mean ventricular CSF values and the non-gaussian component of MAP-MRI (estimated from the b = 2600s/mm^2 images) used to produce 3 further images of: Mean Non-Gaussianity (NG), Non-Gaussianity Perpendicular and Non-Gaussianity Parallel. All images were then normalised to MNI space using SPM12 as described above.

2.4.3. Voxel-based morphometry (VBM)

Computational Analysis Toolbox (CAT12) (Gasar and Dahnke, 2016) was utilized to investigate potential sleep related changes in brain structure and assess whether any potential changes in diffusion are driven by partial volume effects. GM, WM, CSF and total intracranial volume were assessed. VBM analysis was performed on the high-resolution T_1-weighted anatomical images (MPRAGE) collected during the wake and sleep sessions. VBM included: 1.) spatial registration to a reference MNI template brain; 2.) segmentation into GM, WM and CSF; 3.) bias correction of intensity non-uniformities; 4.) segmentations modulated by scaling with the amount of volume changes due to spatial registration. 3D Gaussian smoothing (SPM12) with FWHM=8 mm was applied to the normalized modulated tissue probability maps images prior to the voxel-wise comparison.

2.4.4. Statistical analysis

Physiological measures. Changes in HRV-HF and button press response were investigated. Main effects of time and condition (wake; sleep) and their interaction were assessed using repeated measures ANOVA in SPSS 27 (IBM SPSS Statistics).

DTI/DKI/DKTI. The mean GM and WM (tissue probability> 90%) DTI/DKI/DKTI indices were compared between sessions with a paired-sample T-test (SPSS). We used the false discovery rate (FDR) (Benjamini and Hochberg, 1995) to control for multiple comparison errors when we assessed the statistical significance of global changes in diffusion parameters in GM and WM and also report standardized effect sizes (Cohen's d). Moreover, DKI/DKTI parameters were compared across conditions using voxel-wise paired sample t-test in SPM12. Statistical significance was determined using cluster size inference with an initial cluster forming threshold of $p < 0.001$ (Woo et al., 2014), and cluster $p_{FDR} < 0.05$. Anatomical information was derived using the xjView toolbox (http://www.alivelearn.net/xjview; based on the WFU_PickAtlas, http://fmri.wfubmc.edu/software/PickAtlas).

ROI analysis in ascending arousal network and thalamic nuclei. Paired t-test analysis was carried out to compare mean kurtosis during wake and sleep in the ROIs derived from the Harvard Ascending Arousal Network (AAN) Atlas (Edlow et al., 2012), specifically focusing on Dorsal/Median Raphé and Locus Coeuleus. Dorsal/Median Raphé and Locus Coeruleus ROIs were combined to one cluster before calculating the changes in mean kurtosis. Moreover, the Oxford thalamic connectivity atlas (Behrens et al., 2003) was used to investigate sleep related changes in kurtosis in the thalamic nuclei.

MAP-MRI. To determine whether sleep-associated changes in kurtosis were predominantly driven by water exchange between compartments or by extra/intra-cellular relative volume changes we created mean kurtosis (MK) cluster masks then used these to estimate changes in MSD (sensitive to the overall mobility of intra and extracellular water molecules) and RTOP (sensitive to membrane restriction and intracellular volume). We utilised FDR to control for multiple comparisons. As DKI and MAP-MRI both provide information on non-gaussianity, we additionally compared the sensitivity of DKI and MAP-MRI-NG to sleep-related changes. This was accomplished by qualitative comparison of the voxel-wise statistical significance maps (cluster forming threshold of $p<0.001$, and cluster $p_{FDR}<0.05$) obtained from DKI and MAP-MRI-NG.

VBM.

Total tissue volume. Significant changes in total tissue volume (GM, WM and CSF) were determined by paired sample *t*-test analysis, two-tailed null hypothesis, $p<0.05$ was considered significant.

Voxel-wise comparison. The smoothed (3D Gaussian FWHM=8 mm) modulated normalized tissue probability maps were compared across conditions using voxel-wise paired sample *t*-test in SPM12, where total intracranial volume was used as a covariate. Statistical significance was determined using cluster size inference with an initial cluster forming threshold of $p < 0.001$, and cluster $p_{FDR}<0.05$.

2.4.5. Data and code availability statement

Data and code are available upon request and after the approval of Brighton and Sussex Medical School Research Governance and Ethics Committee.

3. Results

Five participants were excluded from the final analysis: two failed to sleep during the sleep session and three had high motion-related artefacts, leaving a final cohort of 16 participants each scanned twice (once during wake and sleep).

3.1. Behavioural results

3.1.1. PSQI

All participants reported a regular sleep-wake cycle in the preceding month with mean sleep duration, onset latency and efficiency of 7.7 (±1.6) hours, 20.8 (± 12.3) minutes and 95.6 (±2.4)% respectively. Participants also reported good sleep quality with an average PSQI score of 4.3 ± 2.4.

3.1.2. Sleep-induction procedures

Actigraphy indicated good sleep efficiency (80.6% ± 13.1%) prior the wake scan and demonstrated that participants complied well with the pre-scan sleep instructions (see Fig. 1A-B): Mean sleep duration prior to the sleep scan 41min+ 1h51min (of the 16 participants, 14 had no sleep, 1 ~4 h and 1 ~6 h of sleep prior to the sleep scan; of note the latter participants slept well during the sleep scan). Mean sleep duration prior to the wake scan was 6h36min±1h23min; Wilcoxon signed-rank, $Z = 3.533$, $p < 0.001$. Accordingly, participants reported significantly higher sleepiness immediately prior to the sleep (mean KSS= 7.8 ± 0.9) versus the wake scan (KSS = 3.9 ± 1.4); $t_{15} = 9.527$, $p<0.001$).

3.1.3. Sleep during scanning

Participants showed a significant reduction in button press responses during the sleep versus the wake scan indicative of sleep during that scan session: Time x Condition (sleep, wake) interaction $F_{(3, 45)}=9.537$, $p<0.001$ (Fig. 1C). This was supported by a significant increase in parasympathetically mediated HF-HRV during the sleep scan (Time x Condition interaction $F_{(1.735, 26.024)} = 4.773$, $p = 0.021$ after Greenhouse-Geisser correction for lack of sphericity) (Fig. 1D) and self-reported sleep quality during the sleep scan (Fig. 1E).

3.2. Diffusion imaging

None of the standard DTI indices (e.g., MD and FA) showed significant sleep-associated differences in either GM or WM ROIs after Bonferroni correction for multiple comparisons (uncorrected increase in GM FA: $t_{15}=2.16$, $p = 0.024$). However, we did observe significant differences in DKI indices. Specifically, there was a significant decrease in MK in both whole brain GM and WM ($t_{15}=2.82$, $p = 0.006$ and $t_{15}=2.49$, $p = 0.012$ respectively), and RK in both GM and WM ($t_{15}=2.87$, $p = 0.006$ and $t_{15}=2.63$, $p = 0.010$, respectively). Moreover, there was a significant decrease in MKT in both GM and WM ($t_{15}=2.70$, $p = 0.008$ and $t_{15}=2.00$, $p = 0.032$ respectively) though the latter did not survive Bonferroni correction. Notably, MK and MKT values in GM were very similar, though WM MKT produced lower values. A significant increase in KFA was observed in both GM and WM ($t_{15}=2.41$, $p = 0.015$ and $t_{15}=2.30$, $p = 0.018$ respectively). The global diffusion and kurtosis measures are summarised in Table 1, and Supplementary SI-Fig. 1 includes line plots for each measure, with each line representing data from a single participant. Decreases in MK, MKT, and RK in GM and WM were ~1.5%, while the GM increase in KFA was 8.2%.

Similarly, the voxel-based analysis did not show any significant changes for FA and MD. When comparing MK between sleep and wake, several areas of decreased MK during sleep were identified (Fig. 2 blue). Amongst these, 4 clusters survived FDR correction. Significant MK clusters and the corresponding percentage change are summarised in Table 2. The largest significant cluster is located in bilateral posterior and middle cingulate cortex, precuneus, cuneus, and calcarine sulcus. The second largest cluster is centred in the right middle occipital cortex and runs down to the middle temporal lobe. The third cluster is located in the right thalamus (passes through the third ventricle) towards the cerebellum and touches onto the midbrain. The fourth significant cluster (size=182) runs between left thalamus and left superior temporal gyrus.

Brain regions with significantly reduced MK (blue) and RK (red) during sleep. The statistical significance was determined using cluster size inference with an initial cluster forming threshold of $p < 0.001$, where clusters with a corrected FDR of $p < 0.05$ were considered significant. Left side of the image displays axial slices from $z= -20$ to $z = 35$ in 5 mm increments. Right side displays sagittal slices from $x= -50$ to $x = 60$ in 10 mm increments.

Significant decreases in RK were identified in the same areas (Fig. 2 and SI-Table 2). The changes in RK overlap very well with those found with MK, suggesting that the changes in MK are mainly driven by the radial component. No significant changes were observed in the other direction, i.e., increase in diffusion kurtosis during sleep.

In addition to MK and RK, significant KFA clusters (not shown here) also coincide.

Fig. 2 indicated significant reduction in the brainstem. This was confirmed by placing an ROI in the Dorsal/Median Raphé and Locus Coeuleus nuclei, MK was reduced from 0.93 ± 0.05 (wake) to 0.91 ± 0.05 (sleep), $p = 0.0084$, $t_{15} = 2.69$. Moreover, ROI analysis in the thalamus indicated that the greatest reduction in mean kurtosis occured in the nucleus connected to the posterior parietal cortices, where MK was reduced from 0.88 ± 0.04 (wake) to 0.85 ± 0.04 (sleep), $p < 0.0001$, $t_{15} = 6.47$.

3.2.1. MAP-MRI analysis

Table 3 summarises the post-hoc analysis of MAP-MRI parameters MSD and RTOP for the clusters that showed significant reduction in MK during sleep. In all clusters except for the Thalamic cluster, we observed significant reduction in MSD. While all clusters showed a reduction in RTOP, the changes were not significant. Supplementary SI-Figs. 2-5 present cross-correlation matrices summarizing the relationship between MK, RK, MSD, and global CSF change for each significant MK cluster during wake and sleep.

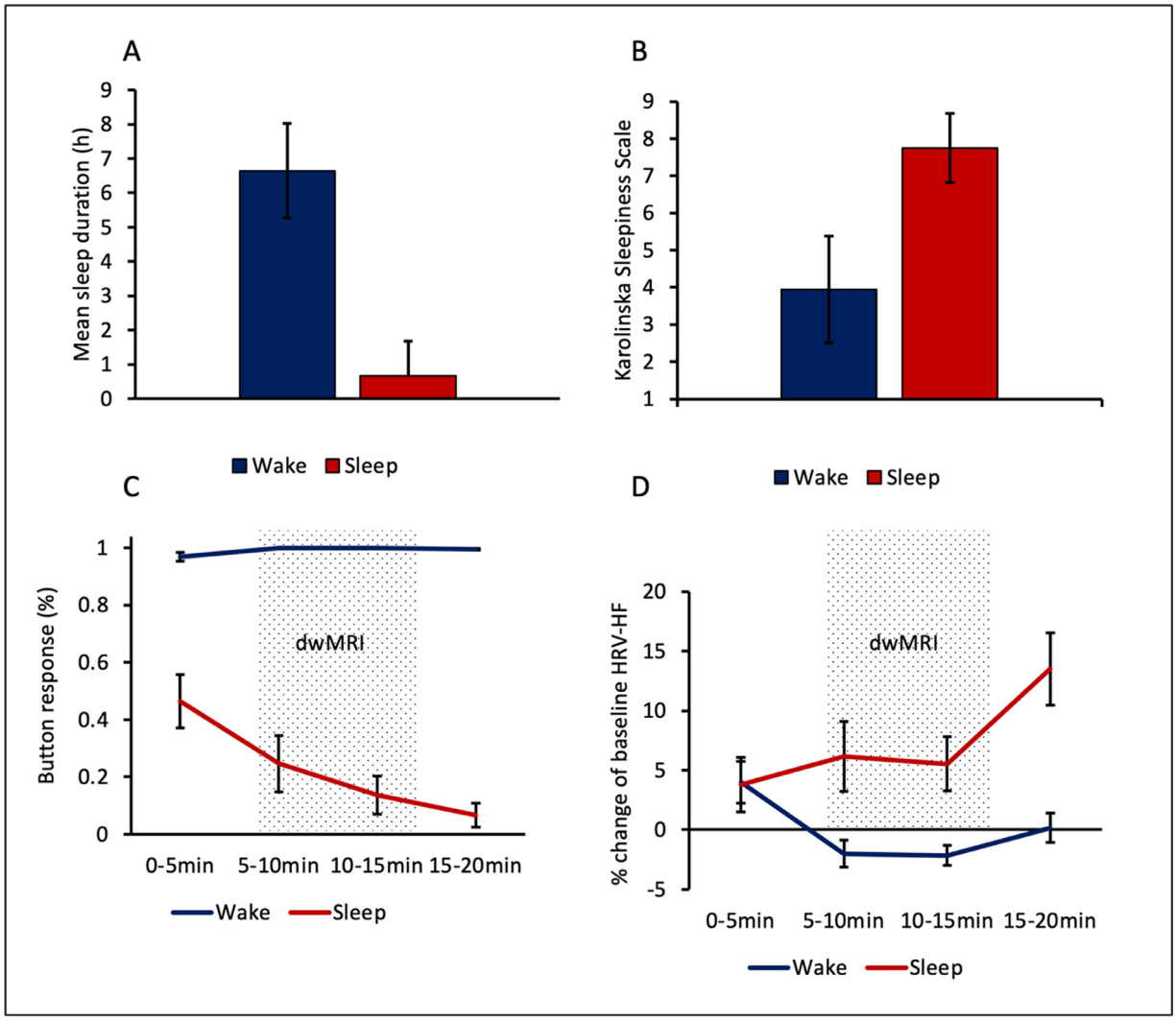

Fig. 1. Behavioural results. **(A)** Mean total sleep time before the wake scan (blue) and sleep scan (red); **(B)** Mean Karolinska sleepiness scale score before scan sessions; **(C)** Button press during the proton scan sessions (sodium not shown here), the dotted area represents the duration of the diffusion scan and the relative position with respect to the start of proton scan; **(D)** High frequency power of HRV during sessions; Error bars = Standard deviation (A and B) and Standard error of the mean (C and D).

Table 1
Summary of mean ± SD of global GM (tissue probability>90%) and WM (tissue probabilty>90%) ROIs diffusion and kurtosis measures.

	GM				WM			
	Wake	Sleep	% change	Cohen's d	Wake	Sleep	% change	Cohen's d
Diffusion measures								
MD ($\mu m^2/ms$)	1.04 ± 0.04	1.04 ± 0.03	−0.40 ± 1.88	0.23	0.90 ± 0.02	0.90 ± 0.01	−0.36 ± 1.76	0.21
AD ($\mu m^2/ms$)	1.17 ± 0.04	1.17 ± 0.03	−0.15 ± 1.60	0.11	1.28 ± 0.01	1.28 ± 0.02	−0.32 ± 1.59	0.21
RD ($\mu m^2/ms$)	0.98 ± 0.04	0.97 ± 0.03	−0.55 ± 2.09	0.28	0.71 ± 0.02	0.71 ± 0.01	−0.40 ± 1.98	0.21
FA	0.12 ± 0.01	0.127 ± 0.01	2.26 ± 4.15*	0.54	0.37 ± 0.01	0.37 ± 0.01	0.29 ± 1.41	0.19
Kurtosis measures (DKI)								
MK	0.71 ± 0.01	0.70 ± 0.02	−1.12 ± 1.58**	0.71	0.94 ± 0.03	0.93 ± 0.03	−1.05 ± 1.68**	0.62
AK	0.68 ± 0.01	0.68 ± 0.02	−0.21 ± 1.62	0.13	0.76 ± 0.02	0.76 ± 0.02	−0.40 ± 1.36	0.30
RK	0.75 ± 0.02	0.74 ± 0.02	−1.63 ± 2.25**	0.72	1.19 ± 0.04	1.17 ± 0.06	−1.41 ± 2.12**	0.66
DKTI								
MKT	0.71 ± 0.01	0.70 ± 0.02	−1.01 ± 1.49**	0.68	0.92 ± 0.02	0.91 ± 0.03	−0.82 ± 1.64*	0.50
KFA	0.20 ± 0.02	0.21 ± 0.02	8.21 ± 13.6**	0.60	0.40 ± 0.02	0.40 ± 0.01	1.87 ± 3.25**	0.57

* Uncorrected statistical significance $p < 0.05$;.

** FDR corrected statistical significance; Cohen's d (Sawilowsky, 2009): $d = 0.01$ very small, $d = 0.20$ small, $d = 0.50$ medium, $d = 0.80$ large, $d = 1.20$ very large and $d = 2.0$ huge effect size.

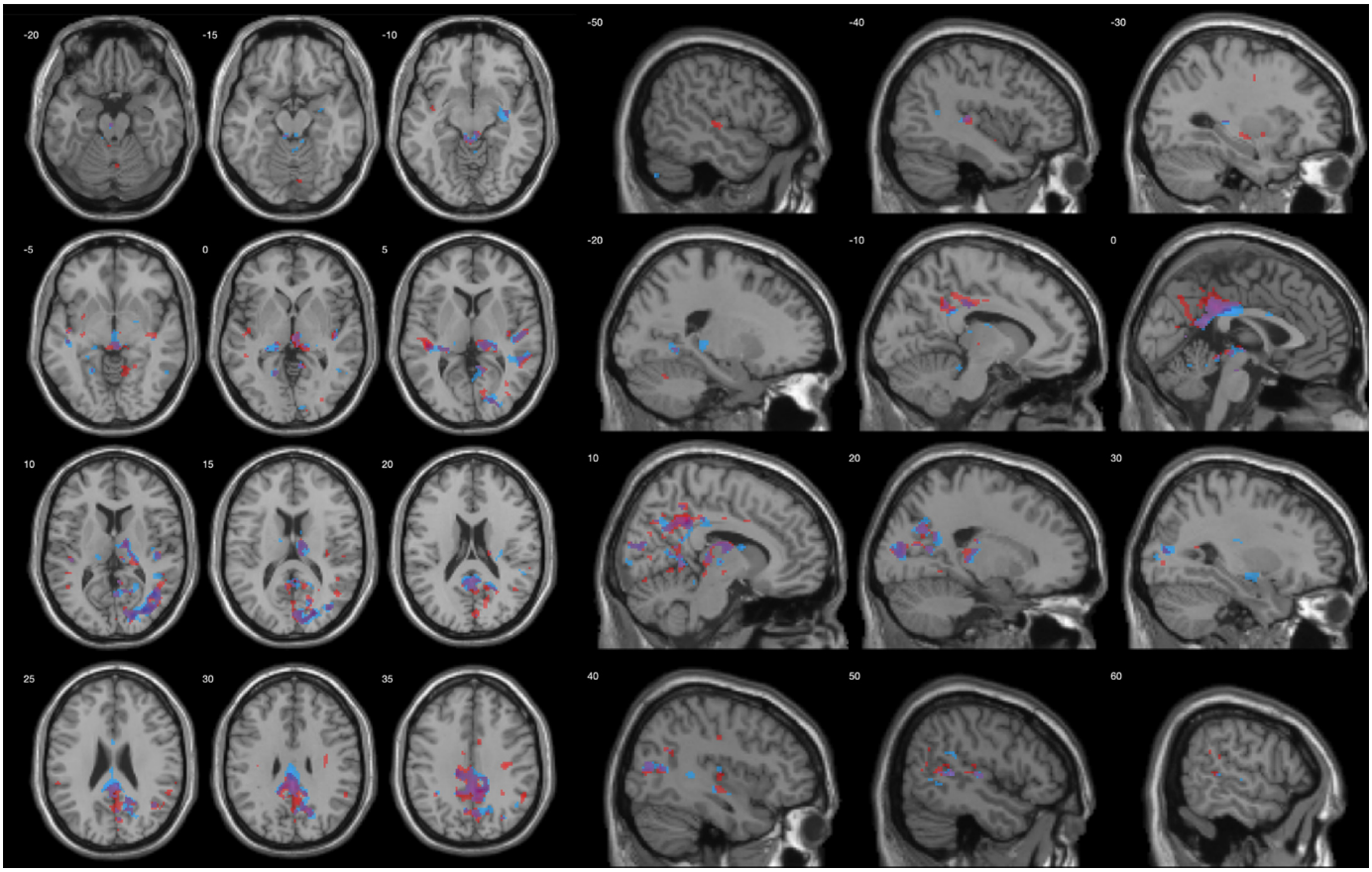

Fig. 2. Voxel-wise comparison of mean and radial kurtosis between wake and sleep.

Table 2
Clusters showing significant reduction in mean kurtosis during sleep.

MK: Brain regions	MNI [x y z]	k	L/R	T value	p (FDR-corr) cluster	% Change of baseline
Middle Occipital	[34 −78 10]	674	R	7.244	0.000	−2.2 ± 1.4
Temporal_Mid_R (aal3v1	[42 −62 10]		R	6.7796		
Cuneus_R (aal3v1)	[22 −84 10]		R	6.4942		
Cingulate_Post_L (aal3v1)	[−8 −38 28]	1868	L	7.0755	0.000	−2.7 ± 1.6
Cingulate_Post_L (aal3v1)	[−4 −46 20]		L	6.9685		
Cingulate_Mid_R (aal3v1)	[0 −28 30]		R	6.9386		
Thal_PuI_R (aal3v1)	[16 −26 2]	590	R	5.7438	0.000	−2.9 ± 1.5
Thal_VL_R (aal3v1	[14 −12 12]		R	5.3819		
Vermis_3 (aal3v1)	[2 −36 −10]		R	5.3425		
Thal_VPL_L (aal3v1)	[−20 −28 2]	182	L	5.5387	0.037	−2.8 ± 1.7
Temporal_Sup_L (aal3v1)	[−42 −26 8]		L	4.8973		
Thal_PuA_L (aal3v1)	[−14 −24 10]		L	4.0985		

Percentage change was determined for each participant before averaging in the following way: ((mean cluster sleep MK- mean cluster wake MK)/mean cluster wake MK) *100; ± represents SD between participants. The statistical significance was determined using cluster size inference with an initial cluster forming threshold of $p < 0.001$, where clusters with FDR- corrected $p < 0.05$ were considered significant.

3.2.2. Sensitivity to sleep-induced changes of DKI and MAP-MRI's non-Gaussianity indices

Both DKI and MAP-MRI were used to measure changes in non-Gaussian diffusion using voxel-wise analysis. Both techniques detected a significant decrease in non-Gaussian diffusion during sleep. However, DKI appears to be more sensitive to the sleep-related changes, as it identified more and larger significant clusters in its statistical maps. Fig. 3 shows the results of comparing changes in non-Gaussian diffusion between wake and sleep states using these techniques. Fig. 3A displays the significant clusters identified using DKI, while Fig. 3B shows the significant non-Gaussian (NG) clusters identified using MAP-MRI.

3.2.3. VBM

There were no significant differences in GM, WM and CSF volumes between wake and sleep scans. The absolute volumes as well as the differences are summarized in Table 4 and plotted in SI-Fig. 6.

The voxel-wise analysis revealed no significant changes in GM volume between the sleep and wake states, and there were also no changes observed at the interface between CSF and GM. However, the analysis did reveal a significant reduction in CSF volume and a corresponding increase in WM volume in the frontal periventricular WM regions.

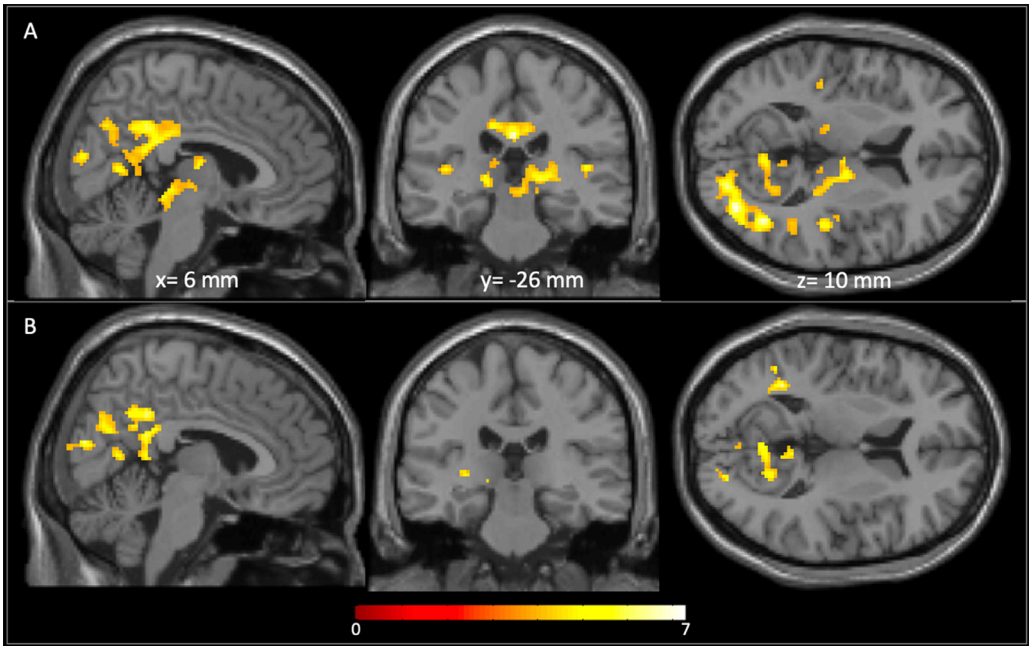

Fig. 3. Assessment of non-Gaussianity. **(A)** Voxel-wise comparison of mean kurtosis (MK) between wake and sleep; **(B)** Voxel-wise comparison of non-Gaussian component of MAP-MRI between wake and sleep. The statistical significance was determined using cluster size inference with an initial cluster forming threshold of $p < 0.001$, where clusters with a corrected FDR of $p < 0.05$ were considered significant. MNI coordinates: $x = 6$ $y = -26$ $z = 10$. The colour bar represents T-value.

4. Discussion

Here, using non-Gaussian diffusion imaging we show that sleep is associated with a global reduction in both mean and radial kurtosis. This reduction in kurtosis (diffusion non-Gaussianity) is in accord with our prior hypothesis, and suggests that the sleep-associated expansion of the interstitial space reported in rodents may also be occurring in humans. In further support of this, we also observed region-wise reductions in radial kurtosis in regions known to be involved in sleep-onset and slow wave generation (e.g., brainstem, thalamus) as well as areas that are highly metabolically active during wakefulness e.g., regions associated with the default mode network (DMN).

Diffusion kurtosis as a measure of deviation from Gaussian diffusion has previously been associated with tissue complexity (Jensen and Helpern, 2010; Szczepankiewicz et al., 2016). The decrease in kurtosis we observed indicates that water diffusion is becoming more Gaussian (Özarslan et al., 2013) during sleep, as would be hypothesised to occur with a sleep-associated increase in the interstitial volume fraction. To further investigate the origin of this reduction in diffusion kurtosis, in particular whether this was likely driven by changes *within* the interstitial domain or alternately an increase in fluid exchange *across* compartments (Jelescu et al., 2022; Olesen et al., 2022) we additionally completed a MAP-MRI analysis. This revealed a sleep-associated reduction in Mean Squared Displacement (MSD) in the significant clusters which would be consistent with a reduction in intracellular volume but not an increase in exchange (which would lead to either no change or an increase in MSD). Furthermore, we also observed a non-significant sleep-associated reduction in the Return-To-Origin-Probability (RTOP) indicative of an increase in the volume of the tissue porous matrix, of which the interstitial space is a component. Indeed, RTOP is a microstructural index inversely correlated to the tissue mean pore volume (Menon et al., 2020). Together, these two observations support the hypothesis that the observed reduction in kurtosis is likely to originate from an increase of the interstitial volume during sleep, in agreement with rodent findings (Xie et al., 2013; Ding et al., 2016). The correlation matrices (Supplementary Figs. 2–5) showed a general negative relationship between MK/RK and MSD across all clusters, but the magnitude of association varies between clusters. This suggests that DKI and MAPMRI may be capturing unique aspects of the brain structure. Additionally, we saw a positive relationship between MSD and CSF volume in the occipital and posterior cingulate clusters, but no relationship with RK. Conversely, there was a positive relationship between MK/RK and CSF volume in the thalamic clusters, but no relationship with MSD. The interpretation of these results may require further study and investigation.

Our VBM did not reveal any significant changes in tissue volumes at the CSF-GM matter interfaces. This supports our interpretation of the diffusion kurtosis findings, indicating that the observed changes in mean kurtosis were not influenced by partial volume changes such as an increase in CSF volume and a reduction in grey matter volume. However, we did find significant changes in the volume of WM and CSF in the frontal periventricular white matter region. Specifically, an increase in WM volume and a corresponding decrease in CSF volume. The significance of these volumetric findings at this point is unclear and requires further investigation, which we defer to future work.

To our knowledge, only one previous study has used diffusion weighted MRI to investigate sleep-associated changes in interstitial volume in humans (Demiral et al., 2019). These authors reported a significant increase in the “slow” ADC of the cerebellum and the temporal lobe and suggested that this may be related to an increase in interstitial volume during sleep. In contrast to this study, we did not observe any significant changes in MD estimated from the DKI analysis. However, this may relate to the greater (~2 fold) sensitivity of kurtosis measures to microstructural changes than diffusivity (Hui et al., 2012) and the fact that ADC (or MD) measurements that use a Gaussian diffusion representation for b values up to 1000s/mm^2 may be biased by unaccounted kurtosis effects. In support of this, DKI representations have also been shown to provide more accurate estimates of ADC (or MD) and other DTI indices (Lanzafame et al., 2016). Additionally, while Demiral et al. (2019) discovered a marked increase in cerebrospinal fluid (CSF) volume (1.3%) during sleep, our findings did not indicate a statistically significant variation in tissue volumes between

Table 3
MAP-MRI results.

	Cuneus cluster				Posterior cingulate cluster				Thalamic cluster				Temporal cluster			
	Wake	Sleep	% change	Cohen's d	Wake	Sleep	% change	Cohen's d	Wake	Sleep	% change	Cohen's d	Wake	Sleep	% change	Cohen's d
MSD (10^{-4})	1.67	1.65	−1.18*	0.61	1.86	1.85	−0.94*	0.45	1.80	1.79	−0.44	0.21	1.47	1.44	−1.63**	0.80
RTOP	11.22	11.03	−0.94	0.19	9.27	9.13	−1.11	0.18	11.34	11.10	−1.54	0.24	13.60	13.43	−0.80	0.14

Summary table of Mean Squared Distance and Return to Origin Probability estimated with the MAP-MRI technique;.
* Uncorrected statistical significance $p< 0.05$;.
** FDR corrected statistical significance; Cohen's d (Sawilowsky, 2009): $d = 0.01$ very small, $d = 0.20$ small, $d = 0.50$ medium, $d = 0.80$ large, $d = 1.20$ very large and $d = 2.0$ huge effect size.

Table 4
Summary of brain tissue volumes during wake and sleep (Mean ± Standard deviation).

		Wake Session	Sleep Session	p-two tailed
Brain Volumes	**GM (ml)**	744.6 ± 78.4	742.1 ± 80.7	0.360
	WM (ml)	544.5 ± 93.0	546.3 ± 90.1	0.167
	CSF (ml)	262.3 ± 36.5	258.6 ± 36.6	0.052

the wake and sleep states. Specifically, we noticed a slight decrease in CSF volume (−0.8%) during sleep, but it was not found to be statistically meaningful.

In addition to predicting a global reduction in GM and WM kurtosis during sleep we also hypothesised that changes would be localised to areas known to exhibit slow wave generation during sleep onset and/or areas such as the default mode network (DMN) that are particularly metabolically active during wakefulness (Raichle et al., 2001). Our regional analyses partially supported this hypothesis, revealing a symmetric pattern with two large clusters showing a reduction in MK/RK that each appeared to form a continuous path, the first running from the right thalamus, along the third ventricle through the midbrain to the cerebellum and the second running from the posterior cingulate gyrus to precuneus and then the cuneus bilaterally. The regions showing a significant decrease in kurtosis have also been functionally related to sleep onset. For example, the thalamus has been shown to be involved in delta rhythm generation via disfacilitation of the cortex (Steriade and Amzica, 1998). Connections between brainstem nuclei and the thalamus are believed to be involved in sleep state switching and the medial thalamus acts as a hub for natural sleep initiation as well as for the initiation of loss of consciousness after anaesthesia (Saper et al., 2010; Baker et al., 2014; Gent et al., 2018). ROI analysis revealed a significant reduction in diffusion kurtosis in the Locus Coeruleus and Raphe nuclei. These findings are particularly intriguing as the Locus Coeruleus is the main source of noradrenaline in the mammalian CNS, a crucial neurotransmitter for attention and arousal (Aston-Jones and Waterhouse, 2016). Noradrenaline has been shown to be a key regulator of the glymphatic system, and reduced noradrenaline signalling has been linked to an expansion of interstitial space and increased cerebrospinal fluid production (Aston-Jones and Waterhouse; Xie et al., 2013; Nilsson et al., 1992). The Raphe nuclei contain serotoninergic neurons, and inhibition of these neurons is associated with decreased anxiety and deep relaxation (Andrade et al., 2013). Furthermore, ROI analysis of Thalamic nuclei showed that the greatest decrease in diffusion kurtosis in the anterior pulvinar and lateral posterior nucleus, which have extensive connections with the posterior parietal cortices (Behrens et al., 2003). While these nuclei are not known to be directly involved in sleep regulation, they are part of the default mode network, which shows particularly high metabolic activity during wake (Raichle et al., 2001).

It is worth noting that while the thalamus and brainstem are involved in sleep onset and slow wave generation, a recent study investigating the haemodynamic response to early stage showed that slow waves of EEG correlated with high frequency haemodynamic fluctuations in frontal areas (Song et al., 2022). On the other hand, sleep spindles correlated with slow haemodynamic fluctuations in the posterior areas (which coincide with our clusters).

The second observed cluster included the posterior cingulate, precuneus, middle temporal gyrus and parietal cortex, key nodes of the DMN that are highly metabolically active during wakefulness (Raichle et al., 2001). These areas have been shown to undergo deactivation during sleep, anaesthesia induced loss of consciousness and vegetative states (Braun 1997; Maquet et al., 1997; Andersson et al., 1998; Fiset et al., 1999; Laureys et al., 1999). Interestingly, precuneus, posterior cingulate and medial parietal cortices are also prone to the effects of sleep deprivation, with reports of a ~1.7% decrease in cortical thickness in these areas after 23 h of sleep deprivation (Elvsåshagen et al., 2017).

The posterior cingulate cortex and precuneus have also been shown to be particularly vulnerable to metabolic challenges i.e., ischaemia and carbon monoxide poisoning and are one of the earliest areas to be affected by Alzheimer's disease (Raichle et al., 2001; DeVolder, 1990; Minoshima et al., 1997) with amyloid beta deposition apparent even in early-stage Alzheimer's disease (Palmqvist et al., 2017). In humans, a single night of sleep deprivation has been shown to significantly reduce amyloid beta clearance (Shokri-Kojori et al., 2018). It is therefore noteworthy that the regions where we observed the most statistically robust sleep-associated reductions in kurtosis co-located with areas that are particularly vulnerable to both metabolic challenges and amyloid deposition in Alzheimer's disease. Based on the local control of sleep homoeostasis these areas might "need" more rest after sleep deprivation this might be the reason for increased glymphatic activity as indicated by significant reduction in kurtosis (Kattler et al., 1994; Krueger and Tononi, 2011).

Sleep-associated reductions in kurtosis also showed a posterior-anterior gradient with greatest reductions observed in posterior regions of the brain. It is therefore noteworthy that a recent study combining MRI and EEG showed increased vasomotor pulsations and slow wave power during early non-rapid eye movement (NREM) sleep in a similar pattern of posterior brain regions (Helakari et al., 2022). Vasomotor pulsation is one of the main pulsatile forces believed to drive CSF flow and promote fluid transport (Yamada et al., 2013; Illif et al., 2013). It is therefore encouraging that an independent group showed plausible glymphatic system related changes in the similar brain areas as us with a completely different MRI technique. Together these observations suggest that during sleep there is increased CSF flux along the perivascular space which is accompanied by the expansion of interstitial space and hence enhanced glymphatic clearance.

4.1. Limitations of the study

Our study has a number of limitations. Firstly, we were unable to decouple the main effects of sleep, sleep deprivation, and use of zolpidem or their interactions. There is currently no data on the effects of zolpidem on diffusion measures. However, per-clinical studies showed that increase in interstitial space volume during sleep is not dependant on how sleep is induced, i.e., naturally or with pharmacological intervention (Xie et al., 2013; Ding et al., 2016). Secondly, we did not observe pre-scan sleep directly but instead relied on actigraphy data to check compliance with the sleep requirements. This showed that all but 2 participants complied with full sleep deprivation, and the 2 participants who showed some sleep during the sleep-deprivation procedure did not differ on indices of sleepiness or sleep during the scan session. A third limitation of the study is an absence of simultaneous EEG recording due to the nature of pulse sequences being used. This meant that we were unable to electrophysiologically confirm sleep in the scanner or directly relate our findings to slow wave activity as has been done in rodents (Xie et al., 2013; Ding et al., 2016; Hablitz et al., 2019). Nevertheless, our indirect measures of sleep during scanning such as loss of muscle tone (button presses) suggests that participants achieved sleep in the scanner. In this regard, muscle tone has previously been used as an approximation for sleep onset (Ogilvie, 2001) and has shown good correlation between sleep onset and stage 2 sleep measured by polysomnography (Viens et al., 1988). It is worth mentioning that our findings are based on cluster level statistics, which is less stringent than voxel-wise correction for multiple comparisons. We chose this approach, as this is the first study investigating the dependency of diffusion gaussianity on sleep, and we wanted to maximise sensitivity, given the relatively small sample size. In order to minimise the risk of false positives, we followed published guidelines for cluster-forming uncorrected threshold (Woo et al., 2014). Finally, we observed that some DKTI parameters, specifically KFA, are very sensitive to noise (particularly in GM). This, however, was not the case for mean and radial kurtosis, on which our findings are reliant.

5. Conclusion

Overall, we report a sleep-associated reduction in diffusional kurtosis in whole brain GM and WM which is consistent with the hypothesis of a relative increase in the interstitial fluid volume fraction during sleep which may facilitate glymphatic clearance. Importantly, we did not observe significant changes in any DTI index, suggesting that kurtosis can be more sensitive than classical diffusion measures to sleep related microstructural changes. Reductions in kurtosis were localised to brain areas associated with slow wave generation (thalamus, brainstem) and default mode network regions, which might be related to an increased glymphatic function during recovery sleep as a result of prolonged activity during wake. Post-hoc analysis with higher-order representations (MAP-MRI) suggests that the observed changes in kurtosis during sleep likely originate from changes in the intra/extracellular domain rather than differences in exchange across compartments i.e. changes in cell membrane permeability.

Founding sources

This study was funded by Sussex Neuroscience and by University of Sussex Research and Development Fund.

Declaration of Competing Interests

None.

Data availability

Data and code are available upon request and after the approval of Brighton and Sussex Medical School Research Governance and Ethics Committee.

Acknowledgments

M.P. is supported by the UKRI Future Leaders Fellowship MR/T020296/2

D.J.D is supported by the UK Dementia Research Institute which receives its funding from DRI Ltd, funded by the UK Medical Research Council, Alzheimer's Society and Alzheimer's Research UK

Supplementary materials

Supplementary material associated with this article can be found, in the online version, at doi:10.1016/j.neuroimage.2023.120124.

References

Aggarwal, M., Smith, M.D., Calabresi, P.A., 2020. Diffusion-time dependence of diffusional kurtosis in the Mouse Brain. Magn. Reson. Med. 84 (3), 1564–1578.
Åkerstedt, T., Gillberg, M., 1990. Subjective and objective sleepiness in the active individual. Int. J. Neurosci. 52 (1–2), 29–37.
Andersson, J., Sotiropoulos, S., 2016. An integrated approach to correction for off-resonance effects and subject movement in diffusion MR imaging. Neuroimage 125, 1063–1078.
Andersson, J., Graham, M., Drobnjak, I., Zhang, H., Filippini, N., Bastiani, M., 2017. Towards a comprehensive framework for movement and distortion correction of diffusion MR images: within volume movement. Neuroimage 152, 450–466.
Andersson, J., Graham, M., Zsoldos, E., Sotiropoulos, S., 2016. Incorporating outlier detection and replacement into a non-parametric framework for movement and distortion correction of diffusion MR images. Neuroimage 141, 556–572.
Andersson, J., Onoe, H., Hetta, J., Lidström, K., Valind, S., Lilja, A., Sundin, A., Fasth, K., Westerberg, G., Broman, J., Watanabe, Y., Långström, B., 1998. Brain networks affected by synchronized sleep visualized by positron emission tomography. J. Cereb. Blood Flow Metab. 18 (7), 701–715.
Arbel-Ornath, M., Hudry, E., Eikermann-Haerter, K., Hou, S., Gregory, J., Zhao, L., Betensky, R., Frosch, M., Greenberg, S., Bacskai, B., 2013. Interstitial fluid drainage is impaired in ischemic stroke and Alzheimer's disease mouse models. Acta Neuropathol. 126 (3), 353–364.
Andrade, T., Zangrossi, H., Graeff, F., 2013. The median raphe nucleus in anxiety revisited. J. Psychopharmacol. 27 (12), 1107–1115.
Aston-Jones, G., Waterhouse, B., 2016. Locus coeruleus: from global projection system to adaptive regulation of behavior. Brain Res. 1645, 75–78.

Baker, R., Gent, T., Yang, Q., Parker, S., Vyssotski, A., Wisden, W., Brickley, S., Franks, N., 2014. Altered activity in the central medial thalamus precedes changes in the Neocortex during transitions into both sleep and Propofol anesthesia. J. Neurosci. 34 (40), 13326–13335.
Behrens, T.E., Johansen-Berg, H., Woolrich, M.W., Smith, S.M., Wheeler-Kingshott, C.A., Boulby, P.A., Barker, G.J., Sillery, E.L., Sheehan, K., Ciccarelli, O., Thompson, A.J., Brady, J.M., Matthews, P.M., 2003. Non-invasive mapping of connections between human thalamus and cortex using diffusion imaging. Nat. Neurosci. 6 (7), 750–757.
Benjamini, Y., Hochberg, Y., 1995. Controlling the false discovery rate: a practical and powerful approach to multiple testing. J. R. Stat. Soc. Series B Stat. Methodol. 57 (1), 289–300.
Berridge, C., Waterhouse, B., 2003. The locus coeruleus–noradrenergic system: modulation of behavioral state and state-dependent cognitive processes. Brain Res. Rev. 42 (1), 33–84.
Braun, A., 1997. Regional cerebral blood flow throughout the sleep-wake cycle. An H2(15)O PET study. Brain 120 (7), 1173–1197.
Buysse, D., Reynolds, C., Monk, T., Berman, S., Kupfer, D., 1989. The Pittsburgh sleep quality index: a new instrument for psychiatric practice and research. Psychiatry Res. 28 (2), 193–213.
Demiral, Ş., Tomasi, D., Sarlls, J., Lee, H., Wiers, C., Zehra, A., Srivastava, T., Ke, K., Shokri-Kojori, E., Freeman, C., Lindgren, E., Ramirez, V., Miller, G., Bandettini, P., Horovitz, S., Wang, G., Benveniste, H., Volkow, N., 2019. Apparent diffusion coefficient changes in human brain during sleep – does it inform on the existence of a glymphatic system? Neuroimage 185, 263–273.
DeVolder, A., 1990. Brain glucose metabolism in postanoxic syndrome. Arch. Neurol. 47 (2), 197.
Ding, F., O'Donnell, J., Xu, Q., Kang, N., Goldman, N., Nedergaard, M., 2016. Changes in the composition of brain interstitial ions control the sleep-wake cycle. Science 352 (6285), 550–555.
Edlow, B., Takahashi, E., Wu, O., Benner, T., Dai, G., Bu, L., Grant, P., Greer, D., Greenberg, S., Kinney, H., Folkerth, R., 2012. Neuroanatomic connectivity of the human ascending arousal system critical to consciousness and its disorders. J. Neuropathol. Exp. Neurol. 71 (6), 531–546.
Eide, P., Ringstad, G., 2015. MRI with intrathecal MRI gadolinium contrast medium administration: a possible method to assess glymphatic function in human brain. Acta Radiol. Short Rep. 4 (11).
Eide, P., Vatnehol, S., Emblem, K., Ringstad, G., 2018. Magnetic resonance imaging provides evidence of glymphatic drainage from human brain to cervical lymph nodes. Sci. Rep. 8 (1).
Elvsåshagen, T., Zak, N., Norbom, L., Pedersen, P., Quraishi, S., Bjørnerud, A., Alnæs, D., Doan, N., Malt, U., Groote, I., Westlye, L., 2017. Evidence for cortical structural plasticity in humans after a day of waking and sleep deprivation. Neuroimage 156, 214–223.
Fick, R., Wassermann, D., Caruyer, E., Deriche, R., 2016. MAPL: tissue microstructure estimation using Laplacian-regularized MAP-MRI and its application to HCP data. Neuroimage 134, 365–385.
Fieremans, E., Novikov, D.S., Jensen, J.H., Helpern, J.A., 2010. Monte Carlo study of a two-compartment exchange model of diffusion. NMR Biomed. 23 (7), 711–724.
Fiset, P., Paus, T., Daloze, T., Plourde, G., Meuret, P., Bonhomme, V., Hajj-Ali, N., Backman, S., Evans, A., 1999. Brain mechanisms of propofol-induced loss of consciousness in humans: a positron emission tomographic study. J. Neurosci. 19 (13), 5506–5513.
Fultz, N., Bonmassar, G., Setsompop, K., Stickgold, R., Rosen, B., Polimeni, J., Lewis, L., 2019. Coupled electrophysiological, hemodynamic, and cerebrospinal fluid oscillations in human sleep. Science 366 (6465), 628–631.
Gaberel, T., Gakuba, C., Goulay, R., De Lizarrondo, S., Hanouz, J., Emery, E., Touze, E., Vivien, D., Gauberti, M., 2014. Impaired Glymphatic perfusion after strokes revealed by contrast-enhanced MRI. Stroke 45 (10), 3092–3096.
Garyfallidis, E., Brett, M., Amirbekian, B., Rokem, A., van der Walt, S., Descoteaux, M., Nimmo-Smith, I., 2014. Dipy, a library for the analysis of diffusion MRI data. Front. Neuroinform. 8.
Gaser, C., Dahnke, R., 2016. CAT- a Computational Anatomy Toolbox For the Analysis of Structural MRI Data. Organization for Human Brain Mapping, Geneva, Switzerland.
Gent, T., Bandarabadi, M., Herrera, C., Adamantidis, A., 2018. Thalamic dual control of sleep and wakefulness. Nat. Neurosci. 21 (7), 974–984.
Grinberg, F., Ciobanu, L., Farrher, E., Shah, N., 2012. Diffusion kurtosis imaging and log-normal distribution function imaging enhance the visualisation of lesions in animal stroke models. NMR Biomed. 25 (11), 1295–1304.
Hablitz, L., Vinitsky, H., Sun, Q., Stæger, F., Sigurdsson, B., Mortensen, K., Lilius, T., Nedergaard, M., 2019. Increased glymphatic influx is correlated with high EEG delta power and low heart rate in mice under anesthesia. Sci. Adv. 5 (2).
Helakari, H., Korhonen, V., Holst, S., Piispala, J., Kallio, M., Väyrynen, T., Huotari, N., Raitamaa, L., Tuunanen, J., Kananen, J., Järvelä, M., Tuovinen, T., Raatikainen, V., Borchardt, V., Kinnunen, H., Nedergaard, M., Kiviniemi, V., 2022. Human NREM sleep promotes brain-wide vasomotor and respiratory pulsations. J. Neurosci. 42 (12), 2503–2515.
Hui, E., Fieremans, E., Jensen, J., Tabesh, A., Feng, W., Bonilha, L., Spampinato, M., Adams, R., Helpern, J., 2012. Stroke assessment with diffusional kurtosis imaging. Stroke 43 (11), 2968–2973.
Iliff, J., Nedergaard, M., 2013. Is there a cerebral lymphatic system? Stroke 44 (6, Supplement 1), S93–S95.
Iliff, J., Chen, M., Plog, B., Zeppenfeld, D., Soltero, M., Yang, L., Singh, I., Deane, R., Nedergaard, M., 2014. Impairment of Glymphatic pathway function promotes tau pathology after traumatic brain injury. J. Neurosci. 34 (49), 16180–16193.
Iliff, J., Wang, M., Liao, Y., Plogg, B., Peng, W., Gundersen, G., Benveniste, H., Vates, G., Deane, R., Goldman, S., Nagelhus, E., Nedergaard, M., 2012. A Paravascular pathway facilitates CSF flow through the brain parenchyma and the clearance of interstitial solutes, including amyloid. Sci. Transl. Med. 4 (147).
Iliff, J., Wang, M., Zeppenfeld, D., Venkataraman, A., Plog, B., Liao, Y., Deane, R., Nedergaard, M., 2013. Cerebral arterial pulsation drives paravascular CSF-interstitial fluid exchange in the murine brain. J. Neurosci. 33 (46), 18190–18199.
Jelescu, I., de Skowronski, A., Geffroy, F., Palombo, M., Novikov, D., 2022. Neurite Exchange Imaging (NEXI): a minimal model of diffusion in gray matter with inter-compartment water exchange. Neuroimage 256, 119277.
Jensen, J., Helpern, J., 2010. MRI quantification of non-Gaussian water diffusion by kurtosis analysis. NMR Biomed. 23 (7), 698–710.
Jensen, J., Falangola, M., Hu, C., Tabesh, A., Rapalino, O., Lo, C., Helpern, J., 2011. Preliminary observations of increased diffusional kurtosis in human brain following recent cerebral infarction. NMR Biomed. 24 (5), 452–457.
Jensen, J., Helpern, J., Ramani, A., Lu, H., Kaczynski, K., 2005. Diffusional kurtosis imaging: the quantification of non-gaussian water diffusion by means of magnetic resonance imaging. Magn. Reson. Med. 53 (6), 1432–1440.
Kattler, H., Dijk, D., Borbély, A., 1994. Effect of unilateral somatosensory stimulation prior to sleep on the sleep EEG in humans. J. Sleep. Res. 3 (3), 159–164.
Lanzafame, S., Giannelli, M., Garaci, F., Floris, R., Duggento, A., Guerrisi, M., Toschi, N., 2016. Differences in Gaussian diffusion tensor imaging and non-Gaussian diffusion kurtosis imaging model-based estimates of diffusion tensor invariants in the human brain. Med. Phys. 43 (5), 2464–2475.
Laureys, S., Goldman, S., Phillips, C., Van Bogaert, P., Aerts, J., Luxen, A., Franck, G., Maquet, P., 1999. Impaired effective cortical connectivity in vegetative state: preliminary investigation using PET. Neuroimage 9 (4), 377–382.
Liao, S., Padera, T., 2013. Lymphatic function and immune regulation in health and disease. Lymphat. Res. Biol. 11 (3), 136–143.
Krueger, J.M., Tononi, G., 2011. Local use-dependent sleep; synthesis of the new paradigm. Curr. Top. Med. Chem. 11 (19), 2490–2492.
Maquet, P., Degueldre, C., Delfiore, G., Aerts, J., Péters, J., Luxen, A., Franck, G., 1997. Functional neuroanatomy of human slow wave sleep. J. Neurosci. 17 (8), 2807–2812.
Menon, V., Gallardo, G., Pinsk, M., Nguyen, V., Li, J., Cai, W., Wassermann, D., 2020. Microstructural organization of human insula is linked to its macrofunctional circuitry and predicts cognitive control. Elife 9.
Minoshima, S., Giordani, B., Berent, S., Frey, K., Foster, N., Kuhl, D., 1997. Metabolic reduction in the posterior cingulate cortex in very early Alzheimer's disease. Ann. Neurol. 42 (1), 85–94.
Monti, J.M., Spence, D.W., Buttoo, K., Pandi-Perumal, S.R., 2017. Zolpidem's use for insomnia. Asian J. Psychiatr. 25, 79–90.
Nedergaard, M., Goldman, S., 2020. Glymphatic failure as a final common pathway to dementia. Science 370 (6512), 50–56.
Nilsson, C., Lindvall-Axelsson, M., Owman, C., 1992. Neuroendocrine regulatory mechanisms in the choroid plexus-cerebrospinal fluid system. Brain Res. Rev. 17 (2), 109–138.
Ogilvie, R., 2001. The process of falling asleep. Sleep Med. Rev. 5 (3), 247–270.
Olesen, J., Østergaard, L., Shemesh, N., Jespersen, S., 2022. Diffusion time dependence, power-law scaling, and exchange in gray matter. Neuroimage 251, 118976.
Osorio-Forero, A., Cherrad, N., Banterle, L., Fernandez, L., Lüthi, A., 2022. When the Locus Coeruleus speaks up in sleep: recent insights, emerging perspectives. Int. J. Mol. Sci. 23 (9), 5028.
Özarslan, E., Koay, C., Shepherd, T., Komlosh, M., İrfanoğlu, M., Pierpaoli, C., Basser, P., 2013. Mean apparent propagator (MAP) MRI: a novel diffusion imaging method for mapping tissue microstructure. Neuroimage 78, 16–32.
Palmqvist, S., Schöll, M., Strandberg, O., Mattsson, N., Stomrud, E., Zetterberg, H., Blennow, K., Landau, S., Jagust, W., Hansson, O., 2017. Earliest accumulation of β-amyloid occurs within the default-mode network and concurrently affects brain connectivity. Nat. Commun. 8 (1).
Peng, W., Achariyar, T., Li, B., Liao, Y., Mestre, H., Hitomi, E., Regan, S., Kasper, T., Peng, S., Ding, F., Benveniste, H., Nedergaard, M., Deane, R., 2016. Suppression of glymphatic fluid transport in a mouse model of Alzheimer's disease. Neurobiol. Dis. 93, 215–225.
Plog, B., Dashnaw, M., Hitomi, E., Peng, W., Liao, Y., Lou, N., Deane, R., Nedergaard, M., 2015. Biomarkers of traumatic injury are transported from brain to blood via the glymphatic system. J. Neurosci. 35 (2), 518–526.
Priest, R., Terzano, M., Parrino, L., Boyer, P., 1997. Efficacy of zolpidem in insomnia. Eur. Psychiatry 12 (S1), 4S–14S.
Raichle, M., MacLeod, A., Snyder, A., Powers, W., Gusnard, D., Shulman, G., 2001. A default mode of brain function. Proc. Natl. Acad. Sci. 98 (2), 676–682.
Reese, T., Heid, O., Weisskoff, R., Wedeen, V., 2003. Reduction of eddy-current-induced distortion in diffusion MRI using a twice-refocused spin echo. Magn. Reson. Med. 49 (1), 177–182.
Ringstad, G., Vatnehol, S., Eide, P., 2017. Glymphatic MRI in idiopathic normal pressure hydrocephalus. Brain 140 (10), 2691–2705.
Saper, C., Fuller, P., Pedersen, N., Lu, J., Scammell, T., 2010. Sleep state switching. Neuron 68 (6), 1023–1042.
Sawilowsky, S.S., 2009. New effect size rules of thumb. J. Mod. Appl. Stat. Methods 8 (2), 597–599.
Shokri-Kojori, E., Wang, G., Wiers, C., Demiral, S., Guo, M., Kim, S., Lindgren, E., Ramirez, V., Zehra, A., Freeman, C., Miller, G., Manza, P., Srivastava, T., De Santi, S., Tomasi, D., Benveniste, H., Volkow, N., 2018. β-Amyloid accumulation in the human brain after one night of sleep deprivation. Proc. Natl. Acad. Sci. 115 (17), 4483–4488.
Song, C., Boly, M., Tagliazucchi, E., Laufs, H., Tononi, G., 2022. fMRI spectral signatures of sleep. Proc. Natl Acad. Sci. 119 (30).
Steriade, M., Amzica, F., 1998. Coalescence of sleep rhythms and their chronology in corticothalamic networks. Sleep Res. Online: SRO 1 (1), 1–10.

Szczepankiewicz, F., van Westen, D., Englund, E., Westin, C., Ståhlberg, F., Lätt, J., Sundgren, P., Nilsson, M., 2016. The link between diffusion MRI and tumor heterogeneity: mapping cell eccentricity and density by diffusional variance decomposition (DIVIDE). Neuroimage 142, 522–532.

Tao, A., Tao, L., Nicholson, C., 2005. Cell cavities increase tortuosity in brain extracellular space. J. Theor. Biol. 234 (4), 525–536.

Taoka, T., Masutani, Y., Kawai, H., Nakane, T., Matsuoka, K., Yasuno, F., Kishimoto, T., Naganawa, S., 2017. Evaluation of glymphatic system activity with the diffusion MR technique: diffusion tensor image analysis along the perivascular space (DTI-ALPS) in Alzheimer's disease cases. Jpn. J. Radiol. 35 (4), 172–178.

Tarasoff-Conway, J.M., Carare, R.O., Osorio, R.S., Glodzik, L., Butler, T., Fieremans, E., Axel, L., Rusinek, H., Nicholson, C., Zlokovic, B.V., Frangione, B., Blennow, K., Ménard, J., Zetterberg, H., Wisniewski, T., de Leon, M.J., 2015. Clearance systems in the brain—implications for Alzheimer disease. Nat. Rev. Neurol. 11 (8), 457–470. doi:10.1038/nrneurol.2015.119.

Viens, M., De Koninck, J., Van den Bergen, H., Audet, R., Christ, G., 1988. A refined switch-activated time monitor for the measurement of sleep-onset latency. Behav. Res. Ther. 26 (3), 271–273.

Woo, C.-.W., Krishnan, A., Wager, T.D., 2014. Cluster-extent based thresholding in fmri analyses: pitfalls and recommendations. Neuroimage 91, 412–419.

Xie, L., Kang, H., Xu, Q., Chen, M., Liao, Y., Thiyagarajan, M., O'Donnell, J., Christensen, D., Nicholson, C., Iliff, J., Takano, T., Deane, R., Nedergaard, M., 2013. Sleep drives metabolite clearance from the adult brain. Science 342 (6156), 373–377.

Yamada, S., Miyazaki, M., Yamashita, Y., Ouyang, C., Yui, M., Nakahashi, M., Shimizu, S., Aoki, I., Morohoshi, Y., McComb, J., 2013. Influence of respiration on cerebrospinal fluid movement using magnetic resonance spin labeling. Fluids Barriers CNS 10 (1), 36.